\$ STORY IN THE STO

Contents lists available at ScienceDirect

Earth and Planetary Science Letters

www.elsevier.com/locate/epsl



Simulation of oxygen isotopes and circulation in a late Carboniferous epicontinental sea with implications for proxy records



Sophia I. Macarewich ^{a,*}, Christopher J. Poulsen ^a, Isabel P. Montañez ^b

- a Department of Earth and Environmental Sciences, University of Michigan, Ann Arbor, 1100 N. University Avenue, Ann Arbor, MI 48109, USA
- ^b Department of Earth and Planetary Sciences, University of California, Davis, One Shields Avenue, Davis, CA 95616, USA

ARTICLE INFO

Article history: Received 9 March 2020 Received in revised form 16 December 2020 Accepted 18 January 2021 Available online 26 January 2021 Editor: L. Derry

Keywords:
epicontinental sea
seawater oxygen isotopes
Carboniferous
seawater circulation
late Paleozoic ice age

ABSTRACT

Reconstructions of ancient ocean chemistry are largely based on geochemical proxies obtained from epicontinental seas. Mounting evidence suggests that these shallow inland seas were chemically distinct from the nearby open ocean, decoupling epicontinental records from broader ocean conditions. Here we use the isotope-enabled Community Earth System Model to evaluate the extent to which the oxygen isotopic composition of the late Carboniferous epicontinental sea, the North American Midcontinent Sea (NAMS), reflects the chemistry of its open-ocean sources and connect epicontinental isotope variability in the sea to large-scale ocean-atmosphere processes. Model results support estuarine-like circulation patterns demonstrated by past empirical studies and suggest that orographic runoff produced decreases in surface seawater δ^{18} O (δ^{18} O_w) of up to \sim 3% between the NAMS and the bordering ocean. Simulated sea surface temperatures are relatively constant across the sea and broadly reproduced from proxybased δ^{18} O paleotemperatures for which model-based values of epicontinental δ^{18} O_w are used, indicating that offshore-onshore variability in surface proxy δ^{18} O is primarily influenced by seawater freshening. Simulated bottom water temperatures in the NAMS are also reproduced from biogenic calcite δ^{18} O using model-based values of epicontinental $\delta^{18}O_w$, suggesting that benthic marine fossil $\delta^{18}O$ is also influenced by seawater freshening and coastal upwelling. In addition, glacial-interglacial variations in nearshore seawater freshening counteract the effects of temperature on marine biogenic δ^{18} O values, suggesting that salinity effects should be considered in δ^{18} O-based estimates of glacioeustatic sea level change from nearshore regions of the NAMS. Our results emphasize the importance of constraining epicontinental dynamics for interpretations of marine biogenic δ^{18} O as proxies of paleotemperature, salinity, and glacioeustasy.

© 2021 Elsevier B.V. All rights reserved.

1. Introduction

Our knowledge of ancient oceans is largely inferred from sedimentary successions deposited in shallow inland seas (i.e. epicontinental, epeiric, marginal, and intracratonic seas; herein referred to as 'epicontinental') reflecting that $\sim\!75\%$ of sedimentary deposits preserved on Earth come from such environments (Peters and Husson, 2017). For the pre-Jurassic (earlier than $\sim\!200$ Ma), the only preserved marine archives are epicontinental due to the subduction of open-marine deposits. The δ^{18} O value of biogenic minerals is dependent on both the oxygen isotope composition and temperature of seawater from which those minerals grew, and thus has been used to construct the history of ocean temperature, sea level, and ice sheet volume over the Phanerozoic and beyond

(Mii et al., 2001; van Geldern et al., 2006). Long-term variation in global compositions of biogenic $\delta^{18}O$ has further fueled debate over whether this trend records a shift in ocean temperatures, the influence of diagenetic alteration, or the evolution of global seawater δ^{18} O (δ^{18} O_w) driven mainly by high-temperature water-rock interactions at mid-ocean ridges (e.g., Gregory and Taylor, 1981; Veizer and Prokoph, 2015). At any timescale, the reconstruction of an oxygen isotope secular curve from epicontinental deposits assumes that these environments were representative of more openocean settings. However, these paleo-seas were much broader than deep (« 200 m) and often semi-restricted, and thus local environmental factors such as climate, freshwater input, and seawater circulation likely altered the chemistry and isotopic composition of these small volumes of seawater relative to contemporaneous oceans (Holmden et al., 1998; Panchuk et al., 2006; Brand et al., 2009; Woodard et al., 2013; Rosenau et al., 2014; Joachimski and Lambert, 2015; Narkiewicz et al., 2017; Montañez et al., 2018; Jimenez et al., 2019). Consequently, local-scale differences in $\delta^{18}O_{W}$

^{*} Corresponding author.

E-mail address: sophmaca@umich.edu (S.I. Macarewich).

may have been superimposed on the global oxygen isotope secular curve.

Geochemical discrepancies between carbonate sediments from epicontinental and more open-marine settings have motivated investigation of the local environmental dynamics that form distinct shallow inland water masses (Holmden et al., 1998; Panchuk et al., 2006; Brand et al., 2009). Numerical constraints, using coupled epeiric sea-ocean carbon box models and salinity mixing models, have helped discern the relative importance of carbon and water fluxes in epicontinental seas and emphasize that observed isotopic variations cannot be reproduced without some terrestrial influence and/or restricted exchange with the open ocean (Panchuk et al., 2005; Roark et al., 2017). The water fluxes that determine values of epicontinental $\delta^{18}O_w$ depend on local surface processes (evaporation and precipitation), freshwater inputs via runoff, and seawater circulation and exchange with the bordering ocean, which are quantities that cannot be directly inferred from biogenic isotope records or box models.

The advantage of applying Earth system models to studies of ancient epicontinental seas is that they can explicitly resolve these hydrologic processes through the physical representation of major components of the Earth system (i.e. atmosphere, ocean, land surface, and sea ice). Simulated patterns of precipitation, temperature, and salinity from Earth system models have been compared with geochemical records from epicontinental seaways to relate local isotopic variations to large-scale climate features, such as monsoonal circulation in the late Paleozoic Donets Sea (Montañez et al., 2018) and orographic precipitation in the Cretaceous Western Interior Seaway (Petersen et al., 2016). Isotope-enabled Earth system models have the added ability to track the isotopic composition of water through the climate system, providing simulated estimates of $\delta^{18}O_w$, which can be directly compared with marine biogenic δ^{18} O values for deriving estimates of temperature, salinity, or glacioeustasy.

The North American Midcontinent Sea (NAMS) was an extensive epicontinental sea that extended from $\sim 10^{\circ} \text{S}-15^{\circ} \text{N}$ and periodically flooded $> 2 \times 10^6 \text{ km}^2$ of the Laurentian Craton during glacioeustatic highstands of the Carboniferous and early Permian (Heckel, 1977; Algeo and Heckel, 2008). Circulation in the sea has long been hypothesized as estuarine, with a low-salinity surface layer positioned over a cooler saltwater wedge, based on multiple lines of geologic evidence, including patterns of total organic carbon and redox-sensitive trace elements, faunal diversity and distribution, and radiogenic isotopes (Algeo and Heckel, 2008; Roark et al., 2017; Turner et al., 2019). The NAMS is an ideal case study for epicontinental sea dynamics because stable isotope records from this region contribute disproportionally to late Carboniferous secular curves and paleoclimate reconstructions (e.g., Grossman et al., 2008; Henkes et al., 2018).

Here we use an isotope-enabled Earth system model to link variations in $\delta^{18}O_w$, temperature, and salinity to the degree of freshwater influence and coastal upwelling in the NAMS. We resolve broad patterns of superestuarine circulation and specifically address the sensitivity of seawater freshening and upwelling influence to changes in regional topography and water column depth, respectively. We compare simulated values and patterns of $\delta^{18}O_w$ and sea temperature with proxy-based paleotemperatures to evaluate the primary environmental drivers of spatial variability in marine biogenic δ^{18} O. We further compare simulated patterns of circulation, temperature, and $\delta^{18}O_{W}$ in the NAMS for a glacioeustatic highstand and for a lowstand to constrain glacialinterglacial changes in ambient temperature and seawater freshening. To our knowledge, this study is the first to synthesize isotopeenabled Earth system modeling and published geochemical proxy data to constrain the regional controls on isotopic compositions and circulation in an ancient epicontinental sea.

2. Methods

We employ the fully coupled isotope-enabled Community Earth System Model version 1.2 (iCESM), a global climate model that has been widely used for future climate prediction and modern climate studies (Hurrell et al., 2013). Coupled simulations using iCESM have been found to compare well to present day observations and paleoclimate records (Zhu et al., 2017; Tabor et al., 2018; Brady et al., 2019; Ladant et al., 2020; Zhu et al., 2020). CESM has been shown to accurately reproduce modern SST differences between marginal seas and the open ocean in the same latitudinal band, providing support for the use of CESM in studies of ancient epicontinental seas (Judd et al., 2020). The fully coupled configuration of iCESM includes the Community Atmosphere Model version 5 (iCAM), Community Land Model version 4 (iCLM), Parallel Ocean Model version 2 (iPOP), and Sea Ice Model version 4 (iCICE) components (Brady et al., 2019). iCAM and iCLM have a $1.9^{\circ} \times 2.5^{\circ}$ horizontal resolution with 30 vertical levels. iPOP and iCICE have a nominal 1° horizontal resolution.

The ocean component of iCESM, iPOP, features an orthogonal grid with an enhancement of meridional resolution near the equator to more precisely simulate low-latitude ocean dynamics such as the El-Niño Southern Oscillation (Griffies et al., 2000). This equatorial grid refinement corresponds to a $0.3^{\circ} \times 1^{\circ}$ horizontal resolution in the NAMS region. iPOP has 60 vertical levels with 10 m resolution in the top 15 levels and is stretched to 250 m resolution for the deepest ocean. In the NAMS, due to the shallow depths of the epicontinental seaway, a maximum of 12 vertical levels (i.e. up to 120 m depth) are used. The iPOP grid resolution captures large-scale features of climate and ocean circulation and relies on parameterizations for unresolved physics, such as upper ocean mixing processes. Vertical mixing is represented using the modified K-Profile Parameterization (KPP) scheme (Danabasoglu et al., 2006) with a horizontally constant background diffusivity of 0.1×10^{-4} m² s⁻¹ to accommodate the deep time paleogeography. The Gent-McWilliams scheme with diagnostically evaluated isopycnal diffusivity, as described in Danabasoglu et al. (2012), is used as the lateral closure with upper ocean isopycnal diffusivity values up to 3000 m² s⁻¹. The horizontal diffusivity coefficient is also set to 3000 m² s⁻¹ in the surface diabatic layer. A detailed description of the ocean model can be found in Danabasoglu et al. (2012).

Riverine discharge is introduced into iPOP with zero salinity as an additional surface flux over a specified region surrounding the actual river mouth, implicitly neglecting any estuarine mixing or exchange (Griffies et al., 2005; Tseng et al., 2016). We implement several changes to the treatment of riverine discharge in iPOP that have been found to improve unresolved estuarine processes and reduce near-shore salinity biases, including (1) removing the contribution of river runoff to the surface buoyancy flux in the KPP and (2) using local salinity and δ^{18} O_W as reference values in the virtual flux formulations (Sun et al., 2019; Tseng et al., 2016).

The simulations presented in this study are branched for 200 years from late Carboniferous interglacial and glacial simulations (not shown here) that were each integrated for \sim 1,500 years to near equilibrium with a 100-yr mean top-of-atmosphere net energy flux of -0.01 and -0.16 W m $^{-2}$, respectively. We use the same continental distribution of a late Pennsylvanian (300 Ma) paleogeography (Domeier and Torsvik, 2014), deep ocean bathymetry, treatment of aerosols, and solar luminosity between the interglacial highstand and glacial lowstand simulations. Deep ocean bathymetry is flat with a basic mid-ocean ridge system defined by accretion zones in the Gplates tectonic reconstruction at 300 Ma (www.gplates.com). Aerosol distributions are zonally averaged separately for land and ocean from pre-industrial levels following the procedure outlined by Heavens et al. (2012). Solar luminosity is reduced to 97.5% of the modern value, in accordance with tra-

Table 1Differences in model boundary conditions between glacioeustatic highstand simulations, which only include NAMS water column depth and elevation of the Central Pangaean Mountains (CPM). Note that the elevation of the CPM is uniformly increased by 100% from *DeepSeaLowMtn* to *DeepSeaHighMtn*. Case names are used to refer to each sensitivity experiment.

Case	NAMS depth	CPM maximum elevation
ShallowSeaLowMtn	Uniform 60 m	2000 m
SlopeSeaLowMtn	Mean 50 m	2000 m
DeepSeaHighMtn	Uniform 120 m	4000 m
DeepSeaLowMtn	Uniform 120 m	2000 m

ditional solar evolution models (Gough, 1981). The simulations differ with respect to atmospheric CO2, tropical vegetation, ice sheets, sea level, and global mean $\delta^{18}O_w$ to represent key differences between interglacial highstand and glacial lowstand conditions. A multi-proxy (10³-10⁴ yr resolution) CO₂ reconstruction was used to specify constant interglacial and glacial atmospheric CO₂ concentrations of 560 ppm and 280 ppm, respectively (Montañez et al., 2016; Richey et al., 2020). The distribution of prescribed vegetation follows the mid-late Pennsylvanian biomes for interglacial and glacial phases (Wilson et al., 2017), where the closest possible composition of modern plant functional types is chosen to represent each biome. The prescribed land ice geographies for interglacial and glacial simulations are based on reconstructions of paleo-glacier extent and ice stream pathways constrained by Carboniferous glacial features and deposits from highlatitude southern Gondwana as well as their and detrital zircon U-Pb geochronology (Griffis et al., 2019a, 2019b). The ocean was initialized with a uniform $\delta^{18}O_w$ of 0%, and final values of the interglacial simulations are offset by -0.5% to account for reduced land ice.

To constrain $\delta^{18}O_{\rm W}$ and circulation patterns in the NAMS during a glacioeustatic highstand, we ran four global climate simulations with different scenarios of regional bathymetry and topography in the NAMS (Table 1). The boundary conditions of the four sensitivity simulations are identical to the late Carboniferous simulation apart from water column depth in the NAMS and regional topographic elevations which are not well constrained. More recent estimates suggest that epicontinental sea depths were on the order of 10s of meters (Algeo and Heckel, 2008) as opposed to 100s of meters (Heckel, 1994, 1977). Accordingly, two of our experiments, DeepSeaLowMtn and ShallowSeaLowMtn, have uniform depths of 120 and 60 m, respectively. A third experiment, Slope-SeaLowMtn, has depths that grade from 30 to 80 m with a mean of ~50 m that most closely reflects current proxy-based estimates (Algeo and Heckel, 2008; Roark et al., 2017). A SW-NE trending equatorial mountain chain, collectively referred to as the Central Pangaean Mountains (CPM), bordered the southern margin of the NAMS. Height estimates of the CPM range from \sim 2,000-4,000 m (Ziegler, 1985). To account for this range of estimates, we raise the elevation of the CPM by 2× in a fourth experiment, DeepSeaHigh-Mtn, that corresponds to an increase in peak elevation from 2,000 to 4,000 m. A fifth experiment of a glacioeustatic lowstand scenario of SlopeSeaLowMtn (referred to as Glacial-SlopeSeaLowMtn) is produced to constrain differences in epicontinental temperature, $\delta^{18}O_{w}$, and circulation patterns during glacial phases of the Pennsylvanian. The CPM height of Glacial-SlopeSeaLowMtn is identical to SlopeSeaLowMtn. The NAMS depth is reduced by 1/2 from that of SlopeSeaLowMtn to a mean depth of ~25 m in Glacial-SlopeSeaLowMtn.

We focus on four domains in the NAMS that capture east-west variation in the sea (i.e. onshore to offshore trends within the sea; herein referred to as onshore-offshore) (Fig. 1B) and use modeled differences in $\delta^{18}{\rm O_w}$, temperature, and circulation between DeepSeaLowMtn, SlopeSeaLowMtn, and ShallowSeaLowMtn cases to

capture the effect of epicontinental sea depth on the influence of upwelled marine water. Differences between *DeepSeaLowMtn* and *DeepSeaHighMtn* cases capture the influence of CPM height on seawater freshening. *Glacial-SlopeSeaLowMtn* and *SlopeSeaLowMtn* are compared to assess glacial-interglacial variability in the NAMS. To equilibrate the upper layers of the ocean, each sensitivity simulation was run for 200 years with the last 50 years used in the analysis presented here (Fig. S1).

3. Results & discussion

3.1. NAMS climate conditions

In our glacioeustatic highstand simulations, prevailing upperlevel northeasterly winds drive upwelling offshore of the NAMS continental margin. Low-level winds bring moist air from the bordering Panthalassic Ocean to the CPM and produce large amounts of orographic precipitation, particularly from March-November when the wind direction shifts from north to west (Fig. S2). The NAMS receives an annual cumulative runoff of \sim 1.7 Sv with \sim 27% and 10% entering the Appalachian Basin (AB) and Midland Basin (MB), respectively; resulting in surface salinities that range from 25-27% in the AB and 32-33% in the MB (Fig. S3). The ranges of seasonal surface salinity are similar in DeepSeaLowTopo, ShallowSeaLowTopo, and SlopeSeaLowTopo (i.e. the scenarios with identical CPMs) due to similar patterns of regional precipitation and runoff (Table S1). The bottom water salinities of ShallowSeaLowTopo and SlopeSeaLowTopo exhibit seasonal variations that are comparable to their surface waters, whereas the bottom water salinity of DeepSeaLowTopo remains at a near-constant marine value of 35‰, reflecting the absence of any freshwater influence at depth with a deeper epicontinental sea (120 m). Despite the seasonality of regional precipitation patterns, concomitant changes in basin-scale salinities are low overall because freshwater inputs are integrated into much larger ocean regions. For example, $\sim 1.2 \times 10^{10} \text{ m}^3$ of total annual runoff and direct precipitation enter the AB in ShallowSeaLowTopo. The upper 30 m of the AB has a volume of $\sim 7.5 \times 10^{12} \text{ m}^3$, so the surface ocean region is roughly $625 \times$ larger than the volume of annual freshwater input. Thus, we focus on mean annual seawater conditions (Table S1). Sea surface temperatures (SSTs) are also relatively stable through the seasons and across the sea, varying between 28 to 31 °C.

3.2. Continental runoff and water column depth control spatial patterns of epicontinental $\delta^{18}O_{\rm w}$

Orographic precipitation from the CPM produces ^{18}O -depleted runoff that flows into the NAMS to produce a laterally extensive surface layer of reduced $\delta^{18}\text{O}_{\text{w}}$ (Fig. 1B). Runoff $\delta^{18}\text{O}$ is influenced by CPM height such that higher elevations produce lower values of runoff $\delta^{18}\text{O}$ and surface $\delta^{18}\text{O}_{\text{w}}$ (Fig. 2A–B). In *DeepSeaLowMtn*, the MB and AB receive runoff with mean annual $\delta^{18}\text{O}$ values of -6.0% and -11.0% that produce surface $\delta^{18}\text{O}_{\text{w}}$ values of -0.8% and -1.8%, respectively. A doubling of CPM elevation in *DeepSeaHigh-Mtn* decreases runoff $\delta^{18}\text{O}$ by -3.0 and -5.0% and surface $\delta^{18}\text{O}_{\text{w}}$ by -0.4 and -1.3% in the MB and AB, respectively. The onshore-offshore increase in surface $\delta^{18}\text{O}_{\text{w}}$ captured in our simulations is comparable to observed variations in conodont $\delta^{18}\text{O}$ from high-stand deposits inferred to have formed during climatically wetter conditions (Joachimski and Lambert, 2015).

Epicontinental sea depth controls the degree of mixing between upwelled marine water and coastal freshwater runoff in the NAMS, and thus offshore-onshore gradients of bottom $\delta^{18}{\rm O_w}$. Upwelled marine water, with a $\delta^{18}{\rm O_w}$ of -0.2%, is enriched relative to local runoff. A deep shelf in DeepSeaLowMtn allows upwelled water to flow freely into the sea such that the bottom layer

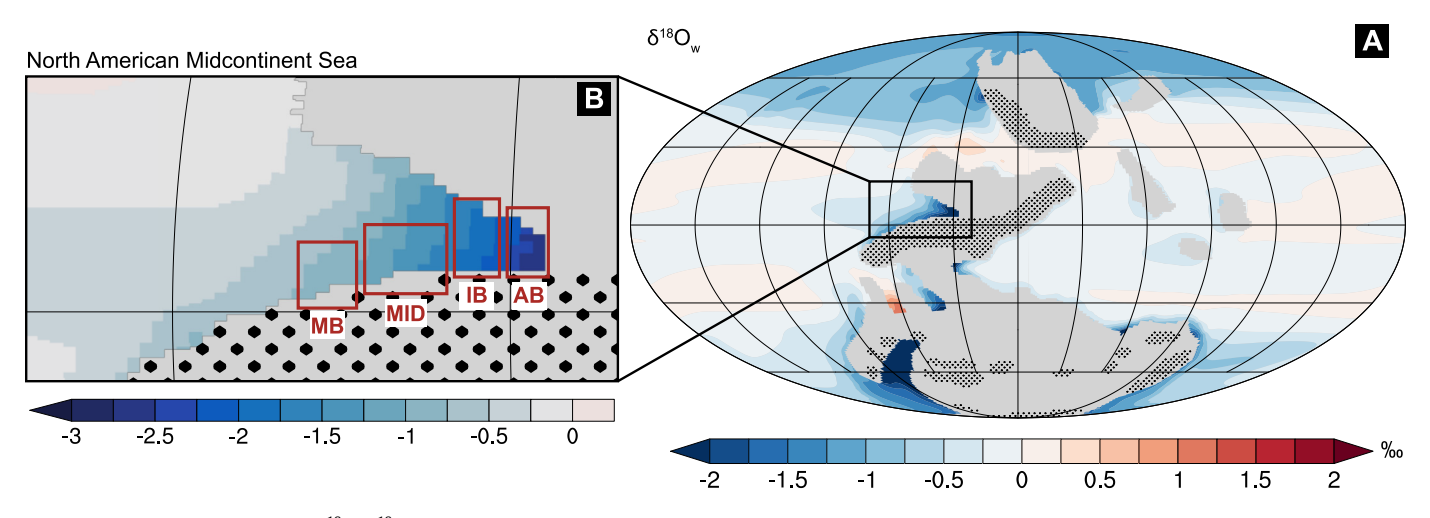


Fig. 1. Global mean annual seawater δ^{18} O (δ^{18} O_w) (A) with a closeup view of the North American Midcontinent Sea (B). Locations of regional domains are marked with red boxes, including the Midland Basin (MB), Midcontinent Shelf (MID), Illinois Basin (IB), and Appalachian Basin (AB). Stippled shading indicates elevations >500 m.

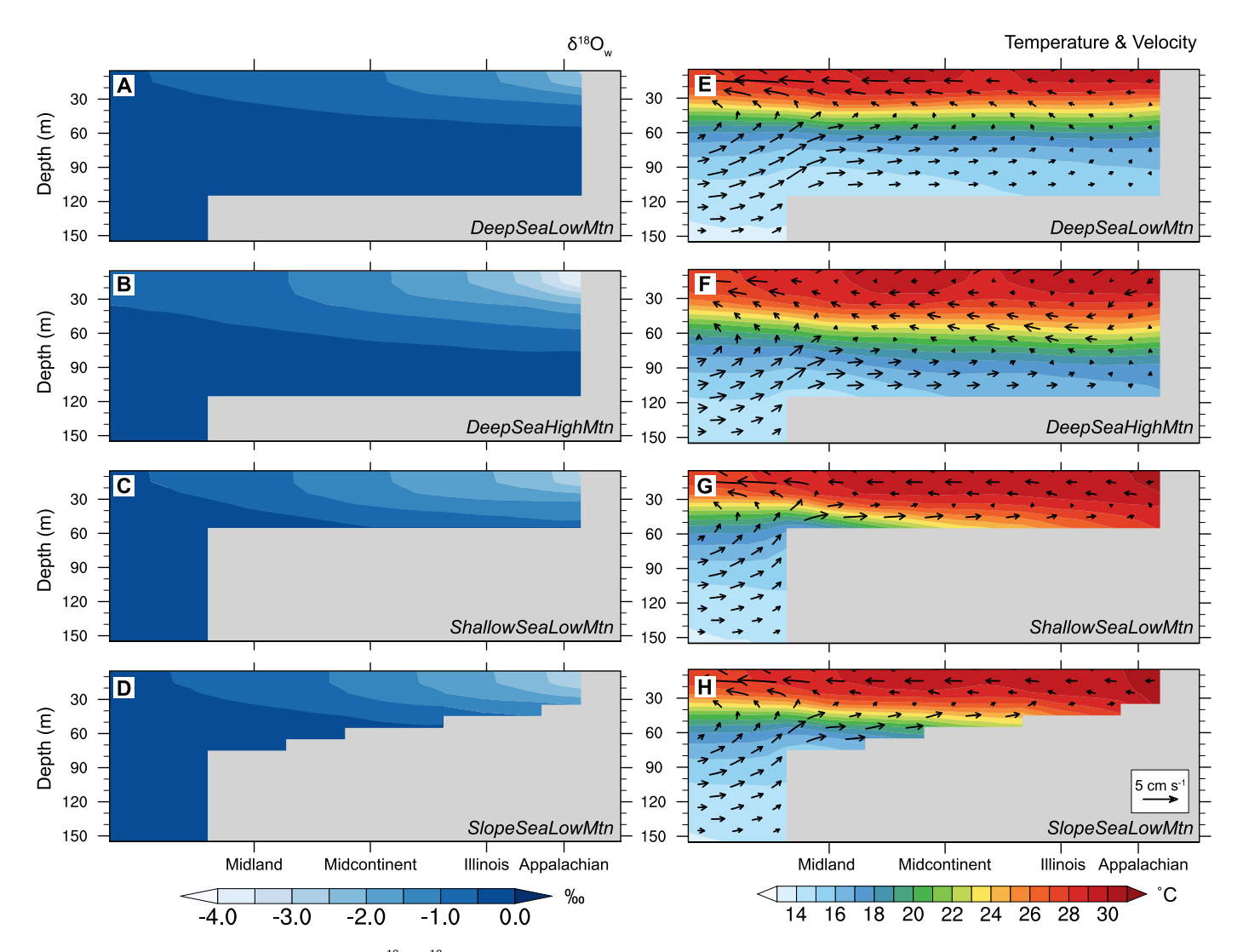


Fig. 2. Longitude-depth cross sections of seawater δ^{18} O (δ^{18} O_w) (A–D) and temperature and velocity (E–H) in the NAMS for each glacioeustatic highstand case. Averages are annual and calculated from 0–10°N. Note that the vertical component of the velocity has been multiplied by a scalar (5,000 cm s⁻¹). The continental shelf is in gray. The surface layer is defined as 0–30 m depth in all cases (based on the mean depth of the regional pycnocline, see Fig. S5), whereas the bottom layer is the greatest 30 m of depth in each case, which is 30–60 m in *ShallowSeaLowMtn*, 90–120 m in *DeepSeaLowMtn* and *DeepSeaHighMtn*, and shallows from 50–80 m to 10–40 m towards the eastern coast in *SlopeSeaLowMtn*.

(90–120 m) is almost entirely marine (Fig. 2A). Shallower depths in ShallowSeaLowMtn inhibit the advection of marine water causing bottom water $\delta^{18} O_{\rm w}$ to be lower by -0.5% in the MB and -1.1% in the AB (Fig. 2C). Marine water in SlopeSeaLowMtn flows inland without freshwater mixing until the edge of the Midcontinent Shelf where a water column depth of \sim 60 m is reached, resulting in $\delta^{18} O_{\rm w}$ similar to the nearby ocean seaward of the shelf edge, whereas interior basins on the shelf (Illinois and Appalachian basins) with shallower depths have lower $\delta^{18} O_{\rm w}$ (Fig. 2D). For ShallowSeaLowMtn and SlopeSeaLowMtn, this produces differences in bottom $\delta^{18} O_{\rm w}$ between the AB and Midcontinent Shelf regions (of \sim 0.4%0 and 1.4%0, respectively) that are comparable to that of well-preserved calcite brachiopod and aragonitic mollusk $\delta^{18} O$ over the same geographic extent (Jimenez et al., 2019; Roark et al., 2017).

3.3. Reconstructing superestuarine circulation

Our simulations generally confirm superestuarine circulation in the NAMS-characterized by estuarine circulation, halocline formation, lateral advection of oxygen-deficient marine deepwater, and a persistent counterclockwise surface gyre (Algeo and Heckel, 2008; Turner et al., 2019). A continent-margin upwelling system draws deeper marine water onto the continental shelf (Fig. 2E-H). High riverine inflow to the eastern end of the sea produces an offshore increase in seawater density that directs counterclockwise circulation of surface waters (Fig. S4). The organization of warmer brackish surface water over cooler marine water forms a highly stratified water column in DeepSeaLowMtn and DeepSeaHighMtn with vertical temperature gradients of >15°C (Fig. 2E-F). Conversely, a reduction of marine influence in ShallowSeaLowMtn and SlopeSeaLowMtn produces lower vertical temperature gradients of \sim 3–5 °C (Fig. 2G–H) that match well with paleotemperatures inferred from coeval conodont and brachiopod δ^{18} O in the AB (Roark et al., 2017).

The formation of extensive black shales in the NAMS has been attributed to low-oxygen bottom waters formed from superestuarine circulation during highstands (Algeo and Heckel, 2008). The depth at which vertical stratification is stable and can form bottom water anoxia is poorly constrained (Montañez and Poulsen, 2013). Our simulations indicate that consistent freshwater input forms a stable pycnocline at a minimum depth of \sim 20-40 m across the NAMS in all cases (Fig. S5). The regional pycnocline extends to the seafloor in the IB and AB of SlopeSeaLowMtn, whereas subpycnoclinal waters in the Midcontinent Shelf and MB approach a marine density of $\sim 1027 \text{ kg m}^{-3}$. The presence of subpycnoclinal marine water in the Midcontinent Shelf of SlopeSeaLowMtn most closely reflects differences found in trace metal enrichment factors between black shale facies of the Midcontinent Shelf and IB (Algeo and Herrmann, 2018). The persistence of a stable pycnocline over the Midcontinent Shelf indicates that water depths of >100 m and approaching depths of the oceanic pycnocline are not necessary for the deposition of black shales.

3.4. Proxy-based paleotemperatures using simulated $\delta^{18}O_W$

Paleo-sea temperature reconstructions using the $\delta^{18} O$ thermometer are complicated by the uncertainty of $\delta^{18} O_w$ in the past. Carbonate clumped isotope measurements are a promising technique for constraining $\delta^{18} O_w$ independently from temperature, but so far have been minimally applied to Late Paleozoic records (Henkes et al., 2018). Without independent constraints on the isotopic composition of ancient seawater, variations in biogenic carbonate and apatite $\delta^{18} O$ have been interpreted with the assumption that epicontinental $\delta^{18} O_w$ was similar to open ocean

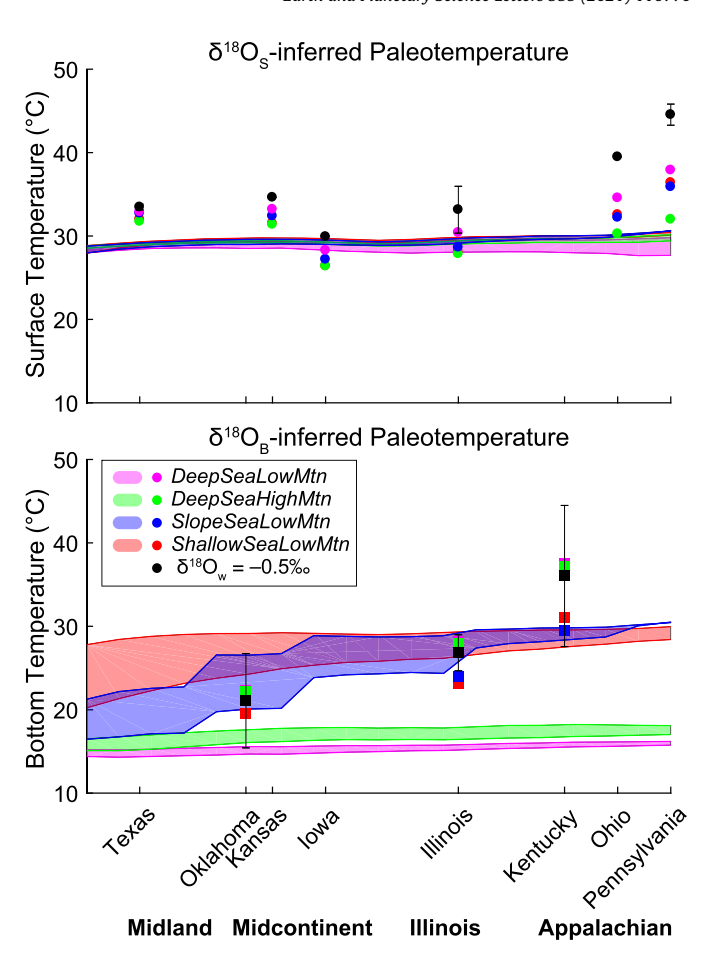


Fig. 3. Comparison of proxy-based paleotemperatures calculated using an openocean $\delta^{18} O_w = -0.5\%$ (black points) and simulated $\delta^{18} O_w$ values (colored points) with simulated sea temperatures from each glacioeustatic highstand case (shaded regions). Shaded temperature regions are averages from 0–10°N at the longitudes of each locality. (A) Conodont data ($\delta^{18} O_{\rm S}$) (Joachimski and Lambert, 2015; Rosenau et al., 2014) are compared to surface temperatures (shaded from 0–30 m depth) using the Pucéat et al. (2010) equation. (B) Brachiopod and mollusk data ($\delta^{18} O_{\rm B}$) (Brand, 1987, 1981; Grossman et al., 2008; Jimenez et al., 2019; Mii et al., 1999) are compared with bottom temperatures (same depths as in Fig. 2 caption) using the Hays and Grossman (1991) equation. Mollusk values are adjusted by -0.8% to directly combine with brachiopod data (see Jimenez et al., 2019). Error bars on the black points are $\pm 1\sigma$ of paleotemperatures derived from proxy data.

values, such as -0.5% for an interglacial world (e.g., Adlis et al., 1988; Mii et al., 1999). However, if applied to paleotemperature equations this assumption produces temperatures of up to $44\,^{\circ}\mathrm{C}$ from highstand deposits in the AB (Fig. 3A), exceeding the lethal limit of most animal phyla (Pörtner, 2002). Several studies have suggested that variations of Pennsylvanian biogenic carbonate and apatite $\delta^{18}\mathrm{O}$ at least partially reflect local salinity changes and cannot be exclusively attributed to temperature and/or high-latitude ice volume (Brand, 1987; Joachimski and Lambert, 2015; Roark et al., 2017; Montañez et al., 2018; Jimenez et al., 2019). However, the degree to which marine biogenic $\delta^{18}\mathrm{O}$ values were influenced by seawater freshening has not been quantitatively examined.

Our simulations provide physical representations of $\delta^{18} O_w$ and temperature that can be used to constrain the proportion of biogenic carbonate and apatite $\delta^{18} O$ variation that is associated with seawater freshening. To illustrate this, we compare onshore-offshore trends in paleotemperatures inferred from Pennsylvanian planktonic conodont and benthic brachiopod and mollusk $\delta^{18} O$ values using simulated $\delta^{18} O_w$ values from each sample locality versus a constant 'open ocean' $\delta^{18} O_w$ value (-0.5%) and, in turn, evaluate the fit between these paleotemperature estimates with simulated temperature patterns. Paleotemperatures calculated

with simulated $\delta^{18} \rm O_{\rm W}$ values indicate that SSTs were lower than paleotemperatures based on using the constant marine $\delta^{18} \rm O_{\rm W}$ value and are generally uniform across the NAMS (Fig. 3A). Using simulated $\delta^{18} \rm O_{\rm W}$ values also improves the agreement between conodont-based paleotemperatures and simulated SSTs. For example, the root mean square error (RMSE) is reduced from 7.6 °C to 2.4 °C when paleotemperatures are calculated using the $\delta^{18} \rm O_{\rm W}$ values from $\it SlopeSeaLowMtn$ (Table S2). Notably, the largest SST changes and greatest improvements in model-data fit occur in the AB where runoff is greatest and $\delta^{18} \rm O_{\rm W}$ is the lowest.

Simulated onshore-offshore variations in $\delta^{18}O_w$ and temperature of near-bottom seawater are controlled by both seawater freshening and upwelled marine water, with marine influence increasing as a function of epicontinental sea depth. Despite similar onshore-offshore trends of $\delta^{18}O_w$ between *ShallowSeaLowMtn* and SlopeSeaLowMtn, the simulated bottom water temperatures of SlopeSeaLowMtn are cooler in the MB and Midcontinent Shelf because the seafloor is deeper. The bottom layers of DeepSeaLowMtn and DeepSeaHighMtn are entirely marine with a near-constant $\delta^{18}O_{w}$ and temperature and therefore cannot account for the observed variation in benthic mollusk and brachiopod δ^{18} O (Fig. 3B). As a result, agreement between simulated bottom water temperatures and proxy-based paleotemperatures using model-based $\delta^{18}O_w$ is best in SlopeSeaLowMtn, as shown by a reduction of RMSE of inferred bottom temperatures from 4.2 °C to 2.0 °C (Table S2). Simulated differences in bottom water conditions between the Midcontinent Shelf and the AB in SlopeSeaLowMtn indicate that \sim 1.4\% (or 30\%) of the onshore-offshore increase in mollusk and brachiopod δ^{18} O of $\sim 5.0\%$ 0 is from decreased seawater freshening and the remainder is from decreased temperatures with greater

Remaining data-model discrepancies may be due to uncertainty of model boundary conditions in deep time and/or model grid resolution. The eastern NAMS, particularly the IB and AB, may have been located to the south of the equator between 310 and 298 Ma (Matthews et al., 2016), rather than flanking the northern margin of the paleoequator as in our experiments. Additionally, the Ancestral Rocky Mountains, located in the northwest of the NAMS, are not included in the simulations presented here. In an additional experiment that assesses the uncertainty in these boundary conditions, we found comparable values of $\delta^{18} O_w$ and temperature (Fig. S6) as well as circulation patterns in the NAMS (Fig. S7). Based on these results, we argue that paleogeographic modifications within the uncertainty of the reconstructions are likely of secondary importance (Lowry et al., 2014). Sub-grid scale paleobathymetric features, such as the Mississippi River Arch (Heckel, 1977), are not resolved at the grid resolution of our simulations, and may lead to local deviations in temperature, $\delta^{18}O_w$, or circulation at individual proxy sites from larger-scale patterns in the NAMS. That said, broad agreement between simulated temperatures and δ^{18} O paleotemperatures using model-based δ^{18} O_w suggest that our simulations sufficiently capture first-order patterns of temperature, $\delta^{18}O_w$, and circulation in the NAMS.

3.5. Glacial-interglacial changes in nearshore seawater freshening rival effects of temperature

Variations of marine biogenic δ^{18} O in Pennsylvanian cyclothems from the NAMS have been used to infer a wide range of sea level fluctuations (30 to 170+ m) (e.g., Adlis et al., 1988; Joachimski et al., 2006; Mazzullo et al., 2007; Rygel et al., 2008; Elrick and Scott, 2010). Differences in marine biogenic δ^{18} O between highstand and lowstand deposits integrate changes in global average δ^{18} O_w, temperature, and local freshwater input over glacial-interglacial cycles that are challenging to differentiate from geochemical data alone. Generally, both high-latitude ice-sheet accumulation and seawater

cooling associated with glacial periods produce higher proxy δ^{18} O values, whereas increased ambient seawater freshening causes a decrease in marine biogenic δ^{18} O. To estimate the contribution of high-latitude ice-sheet volume, and thus glacioeustatic sea level fluctuation, to changes of marine biogenic δ^{18} O, past studies have assumed that glacial-interglacial SST variations were similar to those in the Pleistocene (\sim 2–4 °C) (Waelbroeck et al., 2009) and/or the effects of ambient seawater freshening were negligible (Elrick and Scott, 2010; Joachimski et al., 2006; Adlis et al., 1988). However, these assumptions may not be appropriate for Late Paleozoic glacial-interglacial changes in epicontinental SST and δ^{18} O_w.

Differences between Glacial-SlopeSeaLowMtn and (interglacial) SlopeSeaLowMtn provide an estimate of glacial-interglacial changes in temperature and seawater freshening across the NAMS during the Pennsylvanian. SSTs cool by ~4 °C in the NAMS from the interglacial SlopeSeaLowMtn simulation to the Glacial-SlopeSeaLowMtn simulation (Fig. 4D), which is on the upper end of Pleistocene glacial-interglacial SST differences and would correspond to a \sim 0.8% increase in conodont δ^{18} O (Elrick and Scott, 2010; Joachimski et al., 2006). Glacial-interglacial differences in epicontinental $\delta^{18}O_{\rm w}$ caused by changes in local seawater freshening are spatially disparate, with a slight increase of $\sim 0.1\%_0$ in the MB and decrease of $\sim 0.7\%$ in the Midcontinent Shelf between interglacial and glacial simulations (i.e., SlopeSeaLowMtn vs Glacial-SlopeSeaLowMtn; Fig. 4C). Although the total amount of freshwater runoff received by the NAMS is ~25% less in Glacial-SlopeSeaLowMtn, the degree of seawater freshening is higher in the Midcontinent Shelf in the glacioeustatic lowstand case because a relatively larger amount of cumulative annual runoff (~860 mSv) is directed into this region. Superestuarine circulation patterns break down in the Glacial-SlopeSeaLowMtn simulation with a net onshore transport of surface waters that prevents the oceanward flow of nearshore low-salinity surface waters (Fig. 4D), resulting in slightly higher $\delta^{18}O_w$ in the MB than for the interglacial simulation SlopeSeaLowMtn. The contribution of local seawater freshening to isotopic variation in more offshore regions such as the MB may have been relatively small. Importantly, results from the Midcontinent Shelf suggest that increases in marine biogenic δ^{18} O due to ambient seawater cooling could be almost equally opposed by concomitant decreases in marine biogenic δ^{18} O associated with seawater freshening. These results stress that glacial-interglacial variations in local seawater freshening should be considered in addition to temperature for nearshore regions of epicontinental seas such as the NAMS as such variations in surface $\delta^{18}O_w$ could potentially contribute to increased spread in δ^{18} O-based estimates of glacioeustasy.

4. Modeling limitations

This study represents an important first step in understanding epicontinental sea circulation and oxygen isotope composition. We have shown that isotope-enabled Earth system models such as iCESM are a valuable tool for constraining the local environmental factors that potentially influenced epicontinental $\delta^{18}O_w$, temperature, and circulation in the NAMS and should be considered for investigating other ancient epicontinental seas. It is important to note, however, that our implementation of iCESM has some limitations. High-resolution regional ocean models are able to better represent epicontinental seas by including flow-topography interactions (e.g. bathymetric sills), tidal and near-surface wind-driven mixing processes in estuaries, and other non-steady dynamics. The treatment of riverine freshwater in iPOP as a vertical flux of "augmented precipitation" that is spread over a large region surrounding the river mouth omits any estuarine mixing or exchange processes, and modifications to these river input methods can have an appreciable influence on coastal ocean salinity and stratification (Tseng et al., 2016). The resolution in the upper ocean

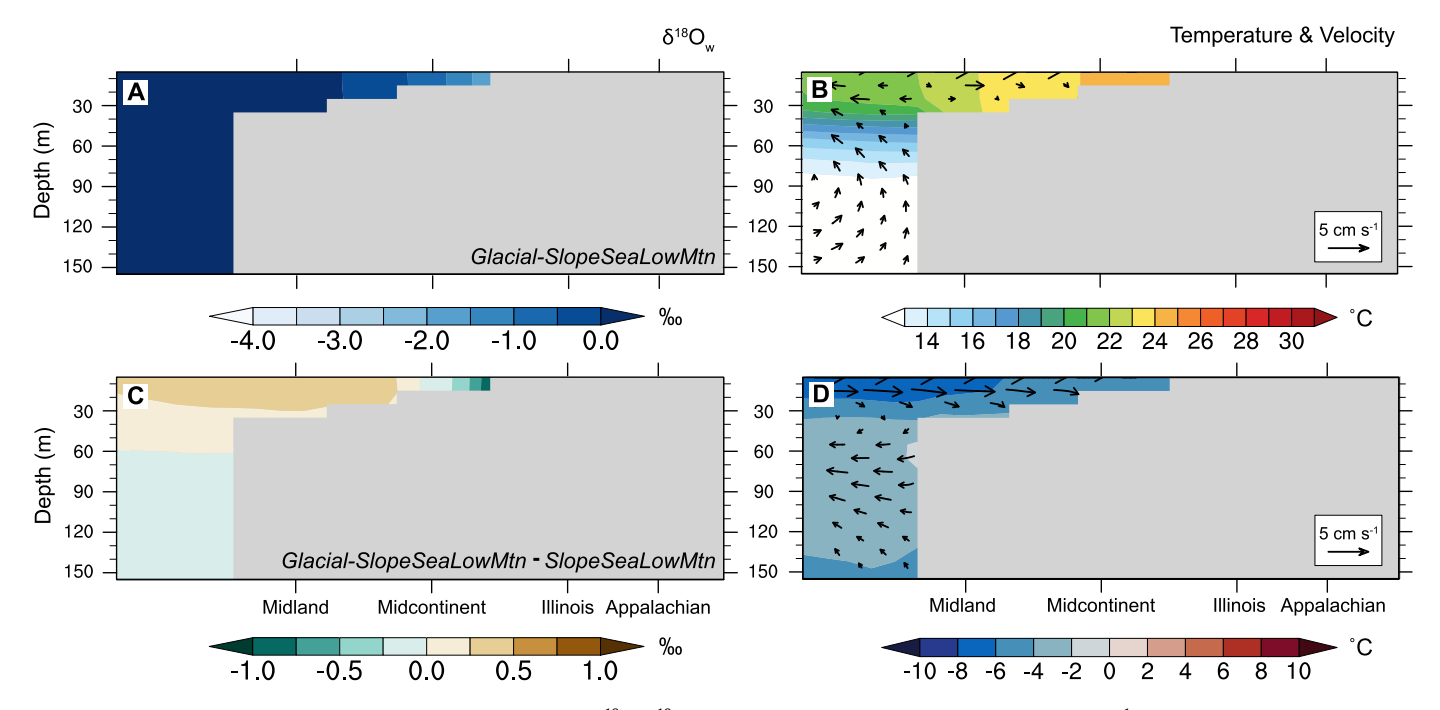


Fig. 4. Longitude-depth cross sections of mean annual (A) seawater δ^{18} O (δ^{18} O_w; ‰) and (B) temperature (°C) and velocity (cm s⁻¹) in the NAMS for a glacioeustatic lowstand (glacial) scenario of *SlopeSeaLowMtn*, or *Glacial-SlopeSeaLowMtn*. Values are calculated as an average from 0–10°N. Note that the vertical component of the velocity has been multiplied by a scalar (5,000 cm s⁻¹) and that the Illinois and Appalachian Basins are above sea level in this case. Differences in mean annual (C) δ^{18} O_w (due to changes in ambient seawater freshening only) and (D) temperature (°C) and velocity (cm s⁻¹) between *SlopeSeaLowMtn* and *Glacial-SlopeSeaLowMtn* are also shown. The continental shelf is in gray.

corresponds to at most 12 vertical levels in the NAMS for the simulations presented here, which may be inadequate for resolving steep vertical gradients in salinity, temperature, and $\delta^{18}O_w$. Consequently, nesting a regional ocean model in an Earth system model or implementing a high-resolution version of iPOP will provide a more complete representation of ancient epicontinental seas. Given the computational cost of high-resolution simulations and the large uncertainty surrounding the NAMS bathymetry, we determined that the ability to run multiple sensitivity simulations in a globally integrated framework (i.e. allowing for dynamic interactions between the open ocean, terrestrial hydrologic cycle, and the NAMS) outweighed the benefit of higher spatial resolution in this first-time modeling study of the NAMS. While the limitations described above may affect the details of our results, we do not believe that they influence the important conclusions of this study.

5. Conclusions & implications

Orographic precipitation from the CPM produces large amounts of freshwater runoff that feed into the NAMS, producing offshoreonshore patterns of decreasing $\delta^{18}O_w$ and superestuarine circulation during glacioeustatic highstands. Offshore-onshore decreases in surface $\delta^{18}O_w$ are enhanced by higher CPM due to the combination of increased continental runoff and decreased values of runoff δ^{18} O. Epicontinental sea depth modifies the degree of mixing between upwelled marine water and surface brackish water, with greater depths enhancing the influence of marine water in the NAMS and thus increasing values of near-bottom $\delta^{18}O_w$. Proxybased δ^{18} O paleotemperatures using simulated values of epicontinental $\delta^{18}O_w$ support that offshore-onshore variation in conodont δ^{18} O is primarily driven by increased proximity to freshwater runoff, whereas brachiopod and mollusk δ^{18} O values are influenced by seawater freshening as well as the presence of upwelled marine water in regions offshore of the Midcontinent Shelf. Glacial-interglacial variation in epicontinental $\delta^{18}O_w$ due to local seawater freshening may be as important as the changes in ambient seawater temperature on marine biogenic δ^{18} O, and thus should be considered in δ^{18} O-based inferences of glacioeustasy from nearshore regions of the NAMS and other comparable epicontinental seas. Notably, patterns of δ^{18} O_w, salinity, and temperature from a simulation with shallow epicontinental depths that deepen towards the continental margin and relatively low-elevation CPM (i.e. SlopeSeaLowMtn) most closely capture the seawater characteristics inferred from published geochemical evidence, and thus provide support for relatively shallow depth in the NAMS.

Negative deviations of low-latitude epicontinental $\delta^{18}O_w$ compared to the nearby open ocean may be relevant to interpretations of the Phanerozoic oxygen isotope secular curve. Records of marine calcite δ^{18} O reveal an \sim 8‰ increase over the past half billion years with two first-order and long debated hypotheses for the origin of this long-term δ^{18} O trend (e.g., Meuhlenbachs and Clayton, 1976; Gregory and Taylor, 1981; Veizer and Prokoph, 2015; Bergmann et al., 2018; Ryb and Eiler, 2018). The first is the progressive increased influence of diagenesis in more deeply buried sedimentary deposits over time (e.g., Land, 1995). The second is a secular increase in global $\delta^{18}O_w$ over the Phanerozoic driven in large part by high-temperature isotopic exchange between seawater and seafloor at mid-ocean ridges (Gregory and Taylor, 1981; Veizer and Prokoph, 2015). In the Phanerozoic, the range of lowlatitude calcite δ^{18} O values increases from between \sim 0 to -4.0%during the Jurassic and Cretaceous to 0 to -12.0% around ~ 200 Mya, with the maximum value remaining $\sim 0\%$ through time. Oceanic crust older than ~200 Mya is not preserved, and thus pre-Jurassic records of calcite δ^{18} O are primarily from low-latitude epicontinental seas (Veizer and Prokoph, 2015). We hypothesize that open-ocean $\delta^{18}O_w$ has remained relatively constant over the past \sim 500 Ma, as evidenced by the absence of values greater than 0\%, and in line with recent studies of clumped isotopes (Bergmann et al., 2018; Rvb and Eiler, 2018). We further suggest that the growing range of calcite δ^{18} O and more negatives values (prior to ~200 Mya) reflect the outsized influence of low-latitude epicontinental seas in marine records that have been impacted by freshwater runoff and diagenetic overprinting. Furthermore, we show that spatial variation of bottom $\delta^{18}{\rm O_W}$ and temperature in a low-latitude epicontinental sea such as the NAMS can account for calcite $\delta^{18}{\rm O}$ values as low as -5.0%. Even lower values of $\delta^{18}{\rm O_W}$ in epicontinental seas could result from shallower sea depths than used for our simulations due to increased seawater freshening. That said, biogenic calcite $\delta^{18}{\rm O}$ values less than -5.0% are challenging to argue as archiving seawater conditions and rather likely carry the overprinting signature of diagenetic alteration.

CRediT authorship contribution statement

Sophia I. Macarewich: Formal analysis, Methodology, Software, Visualization, Writing – original draft. **Christopher J. Poulsen:** Conceptualization, Writing – review & editing. **Isabel P. Montañez:** Conceptualization, Writing – review & editing.

Declaration of competing interest

The authors declare that they have no known competing financial interests or personal relationships that could have appeared to influence the work reported in this paper.

Acknowledgements

This work was supported by the National Science Foundation (NSF) awards 1338200 (C.J.P.) and 1338281 (I.P.M.). We thank members of the Poulsen lab for helpful discussion. We also acknowledge high-performance computing support from Cheyenne (doi:10.5065/D6RX99HX) provided by the National Center for Atmospheric Research's Computational and Information Systems Laboratory, sponsored by NSF.

Appendix A. Supplementary material

Supplementary material related to this article can be found online at https://doi.org/10.1016/j.epsl.2021.116770.

References

- Adlis, D.S., Grossman, E.L., Yancey, T.E., McLerran, R.D., 1988. Isotope stratigraphy and paleodepth changes of Pennsylvanian cyclical sedimentary deposits. Palaios 3, 487–506. https://doi.org/10.2307/3514722.
- Algeo, T.J., Heckel, P.H., 2008. The Late Pennsylvanian Midcontinent Sea of North America: a review. Palaeogeogr. Palaeoclimatol. Palaeoecol. 268, 205–221. https://doi.org/10.1016/j.palaeo.2008.03.049.
- Algeo, T.J., Herrmann, A.D., 2018. An ancient estuarine-circulation nutrient trap: the Late Pennsylvanian Midcontinent Sea of North America. Geology 46, 143–146. https://doi.org/10.1130/G39804.1.
- Bergmann, K.D., Finnegan, S., Creel, R., Eiler, J.M., Hughes, N.C., Popov, L.E., Fischer, W.W., 2018. A paired apatite and calcite clumped isotope thermometry approach to estimating Cambro-Ordovician seawater temperatures and isotopic composition. Geochim. Cosmochim. Acta 224, 18–41. https://doi.org/10.1016/j.gca.2017.11.015.
- Brady, E., Stevenson, S., Bailey, D., Liu, Z., Noone, D., Nusbaumer, J., Otto-Bliesner, B.L., Tabor, C., Tomas, R., Wong, T., Zhang, J., Zhu, J., 2019. The connected isotopic water cycle in the Community Earth System Model Version 1. J. Adv. Model. Earth Syst. 11, 2547–2566. https://doi.org/10.1029/2019MS001663.
- Brand, U., 1981. Mineralogy and chemistry of the lower Pennsylvanian Kendrick fauna, eastern Kentucky: 1. Trace elements. Chem. Geol. 32, 1–16. https:// doi.org/10.1016/0009-2541(81)90124-8.
- Brand, U., 1987. Depositional analysis of the Breathitt Formation's marine horizons, Kentucky, U.S.A.: trace elements and stable isotopes. Chem. Geol. 65, 117–136. https://doi.org/10.1016/0168-9622(87)90068-6.
- Brand, U., Tazawa, J.I., Sano, H., Azmy, K., Lee, X., 2009. Is mid-late Paleozoic oceanwater chemistry coupled with epeiric seawater isotope records? Geology 37, 823–826. https://doi.org/10.1130/G30038A.1.
- Danabasoglu, G., Bates, S.C., Briegleb, B.P., Jayne, S.R., Jochum, M., Large, W.G., Peacock, S., Yeager, S.G., 2012. The CCSM4 ocean component. J. Climate 25, 1361–1389. https://doi.org/10.1175/JCLI-D-11-00091.1.

- Danabasoglu, G., Large, W.G., Tribbia, J.J., Gent, P.R., Briegleb, B.P., McWilliams, J.C., 2006. Diurnal coupling in the tropical oceans of CCSM3. J. Climate 19, 2347–2365. https://doi.org/10.1175/JCLI3739.1.
- Domeier, M., Torsvik, T.H., 2014. Plate tectonics in the Late Paleozoic. Geosci. Front. 5, 303–350. https://doi.org/10.1016/j.gsf.2014.01.002.
- Elrick, M., Scott, L.A., 2010. Carbon and oxygen isotope evidence for high-frequency (10⁴-10⁵ yr) and My-scale glacio-eustasy in Middle Pennsylvanian cyclic carbonates (Gray Mesa Formation), central New Mexico. Palaeogeogr. Palaeoclimatol. Palaeoecol. 285, 307–320. https://doi.org/10.1016/j.palaeo.2009.11.023.
- Gough, D.O., 1981. Solar interior structure and luminosity variations. Sol. Phys. 74, 21–34. https://doi.org/10.1007/BF00151270.
- Gregory, R.T., Taylor, H.P., 1981. An oxygen isotope profile in a section of Cretaceous oceanic crust, Samail Ophiolite, Oman: evidence for δ¹⁸O buffering of the oceans by deep (>5 km) seawater-hydrothermal circulation at mid-ocean ridges. J. Geophys. Res., Solid Earth 86, 2737–2755. https://doi.org/10.1029/jb086ib04p02737.
- Griffies, S.M., Gnanadesikan, A., Dixon, K.W., Dunne, J.P., Gerdes, R., Harrison, M.J., Rosati, A., Russell, J.L., Samuels, B.L., Spelman, M.J., Winton, M., Zhang, R., 2005. Formulation of an ocean model for global climate simulations. Ocean Sci. 1, 45–79. https://doi.org/10.5194/os-1-45-2005.
- Griffies, S.M., Pacanowski, R.C., Hallberg, R.W., 2000. Spurious diapycnal mixing associated with advection in a z-coordinate ocean model. Mon. Weather Rev. 128, 538–564. https://doi.org/10.1175/1520-0493(2000)128<0538:SDMAWA>2.0.CO;
- Griffis, N.P., Montañez, I.P., Fedorchuk, N., Isbell, J., Mundil, R., Vesely, F., Weinshultz, L., Iannuzzi, R., Gulbranson, E., Taboada, A., Pagani, A., Sanborn, M.E., Huyskens, M., Wimpenny, J., Linol, B., Yin, Q.Z., 2019a. Isotopes to ice: constraining provenance of glacial deposits and ice centers in west-central Gondwana. Palaeogeogr. Palaeoclimatol. Palaeoecol. 531, 31–182. https://doi.org/10.1016/j.palaeo.2018.04.020.
- Griffis, N.P., Montañez, I.P., Mundil, R., Richey, J., Isbell, J., Fedorchuk, N., Linol, B., Iannuzzi, R., Vesely, F., Mottin, T., da Rosa, E., Keller, B., Yin, Q., 2019b. Coupled stratigraphic and U-Pb zircon age constraints on the late Paleozoic icehouse-to-greenhouse turnover in south-central Gondwana. Geology 47, 1146–1150. https://doi.org/10.1130/G46740.1.
- Grossman, E.L., Yancey, T.E., Jones, T.E., Bruckschen, P., Chuvashov, B., Mazzullo, S.J., Mii, H., 2008. Glaciation, aridification, and carbon sequestration in the Permo-Carboniferous: the isotopic record from low latitudes. Palaeogeogr. Palaeoclimatol. Palaeoecol. 268, 222–233. https://doi.org/10.1016/j.palaeo.2008.03.053.
- Hays, P.D., Grossman, E.L., 1991. Oxygen isotopes in meteoric calcite cements as indicators of continental paleoclimate. Geology 19, 441–444.
- Heavens, N.G., Shields, C.A., Mahowald, N.M., 2012. A paleogeographic approach to aerosol prescription in simulations of deep time climate. J. Adv. Model. Earth Syst. 4. https://doi.org/10.1029/2012MS000166.
- Heckel, P.H., 1977. Origin of phosphatic black shale facies in Pennsylvanian cyclothems of Mid-Continent North America. Am. Assoc. Pet. Geol. Bull. 61, 1045–1068.
- Heckel, P.H., 1994. Evaluation of evidence for glacio-eustatic control over marine Pennsylvanian cyclothems in North America and consideration of possible tectonic effects. In: Dennison, J.M., Ettensohn, F.R. (Eds.), Tectonic and Eustatic Controls on Sedimentary Cycles. SEPM Society for Sedimentary Geology, pp. 65–87.
- Henkes, G.A., Passey, B.H., Grossman, E.L., Shenton, B.J., Yancey, T.E., Pérez-Huerta, A., 2018. Temperature evolution and the oxygen isotope composition of Phanerozoic oceans from carbonate clumped isotope thermometry. Earth Planet. Sci. Lett. 490, 40–50. https://doi.org/10.1016/j.epsl.2018.02.001.
- Holmden, C., Creaser, R.A., Muehlenbachs, K., Leslie, S.A., Bergström, S.M., 1998. Isotopic evidence for geochemical decoupling between ancient epeiric seas and bordering oceans: implications for secular curves. Geology 26, 567–570. https://doi.org/10.1130/0091-7613(1998)026<0567:IEFGDB>2.3.CO;2.
- Hurrell, J.W., Holland, M.M., Gent, P.R., Ghan, S., Kay, J.E., Kushner, P.J., Lamarque, J.F., Large, W.G., Lawrence, D., Lindsay, K., Lipscomb, W.H., Long, M.C., Mahowald, N., Marsh, D.R., Neale, R.B., Rasch, P., Vavrus, S., Vertenstein, M., Bader, D., Collins, W.D., Hack, J.J., Kiehl, J., Marshall, S., 2013. The community earth system model: a framework for collaborative research. Bull. Am. Meteorol. Soc. 94, 1339–1360. https://doi.org/10.1175/BAMS-D-12-00121.1.
- Jimenez, M.Y., Ivany, L.C., Judd, E.J., Henkes, G., 2019. Low and seasonally variable salinity in the Pennsylvanian equatorial Appalachian Basin. Earth Planet. Sci. Lett. 519, 182–191. https://doi.org/10.1016/j.epsl.2019.04.051.
- Joachimski, M.M., Lambert, L.L., 2015. Salinity contrast in the US Midcontinent Sea during Pennsylvanian glacio-eustatic highstands: evidence from conodont apatite δ¹⁸O. Palaeogeogr. Palaeoclimatol. Palaeoecol. 433, 71–80. https://doi.org/ 10.1016/j.palaeo.2015.05.014.
- Joachimski, M.M., von Bitter, P.H., Buggisch, W., 2006. Constraints on Pennsylvanian glacioeustatic sea-level changes using oxygen isotopes of conodont apatite. Geology 34, 277–280. https://doi.org/10.1130/G22198.1.
- Judd, E.J., Bhattacharya, T., Ivany, L.C., 2020. A dynamical framework for interpreting ancient sea surface temperatures. Geophys. Res. Lett. https://doi.org/10.1029/ 2020GI 089044
- Ladant, J.B., Poulsen, C.J., Fluteau, F., Tabor, C.R., Macleod, K.G., Martin, E.E., Haynes, S.J., Rostami, M.A., 2020. Paleogeographic controls on the evolution of Late Cretaceous ocean circulation. Clim. Past 16, 973–1006. https://doi.org/10.5194/cp-16-973-2020.

- Land, L.S., 1995. Comment on "Oxygen and carbon isotopic composition of Ordovician brachiopods: implications for coeval seawater" by H. Qing and J. Veizer. Geochim. Cosmochim. Acta 59, 2843–2844. https://doi.org/10.1016/0016-7037(95)00176-7.
- Lowry, D.P., Poulsen, C.J., Horton, D.E., Torsvik, T.H., Pollard, D., 2014. Thresholds for Paleozoic ice sheet initiation. Geology 42, 627–630. https://doi.org/10.1130/ G35615.1.
- Matthews, K.J., Maloney, K.T., Zahirovic, S., Williams, S.E., Seton, M., Müller, R.D., 2016. Global plate boundary evolution and kinematics since the late Paleozoic. Glob. Planet. Change. https://doi.org/10.1016/j.gloplacha.2016.10.002.
- Mazzullo, S.J., Boardman, D.R., Grossman, E.L., Dimmick-Wells, K., 2007. Oxygencarbon isotope stratigraphy of upper Carboniferous to lower Permian marine deposits in Midcontinent U.S.A. (Kansas and NE Oklahoma): implications for sea water chemistry and depositional cyclicity. Carbon. Evapor. 22, 55–72. https:// doi.org/10.1007/BF03175846.
- Meuhlenbachs, K., Clayton, R.N., 1976. Oxygen isotope composition of the oceanic crust and its bearing on seawater. J. Geophys. Res. 81, 4365–4369. https://doi. org/10.1029/JB081i023p04365.
- Mii, H.S., Grossman, E.L., Yancey, T.E., 1999. Carboniferous isotope stratigraphies of North America: implications for Carboniferous paleoceanography and Mississippian glaciation. Bull. Geol. Soc. Am. 111, 960–973. https://doi.org/10.1130/0016-7606(1999)111<0960:CISONA>2.3.CO;2.
- Mii, H.S., Grossman, E.L., Yancey, T.E., Chuvashov, B., Egorov, A., 2001. Isotopic records of brachiopod shells from the Russian Platform - evidence for the onset of mid-Carboniferous glaciation. Chem. Geol. 175, 133–147. https://doi.org/ 10.1016/S0009-2541(00)00366-1.
- Montañez, I.P., McElwain, J.C., Poulsen, C.J., White, J.D., Dimichele, W.A., Wilson, J.P., Griggs, G., Hren, M.T., 2016. Climate, pCO₂ and terrestrial carbon cycle linkages during late Palaeozoic glacial-interglacial cycles. Nat. Geosci. 9, 824–828. https://doi.org/10.1038/ngeo2822.
- Montañez, I.P., Osleger, D.J., Chen, J., Wortham, B.E., Stamm, R.G., Nemyrovska, T.I., Griffin, J.M., Poletaev, V.I., Wardlaw, B.R., 2018. Carboniferous climate teleconnections archived in coupled bioapatite δ¹⁸O_{PO4} and ⁸⁷Sr/⁸⁶Sr records from the epicontinental Donets Basin, Ukraine. Earth Planet. Sci. Lett. 492, 89–101. https://doi.org/10.1016/j.epsl.2018.03.051.
- Montañez, I.P., Poulsen, C.J., 2013. The late Paleozoic ice age: an evolving paradigm. Annu. Rev. Earth Planet. Sci. 41, 629–656. https://doi.org/10.1146/annurev.earth. 031208.100118.
- Narkiewicz, M., Narkiewicz, K., Krzeminska, E., Kruchek, S.A., 2017. Oxygen isotopic composition of Conodont apatite in the equatorial epeiric Belarussian Basin (Eifelian) relationship to fluctuating seawater salinity and temperature. Palaios 32, 439–447. https://doi.org/10.2110/palo.2016.059.
- Panchuk, K.M., Holmden, C., Kump, L.R., 2005. Sensitivity of the epeiric sea carbon isotope record to local-scale carbon cycle processes: tales from the Mohawkian Sea. Palaeogeogr. Palaeoclimatol. Palaeoecol. 228, 320–337. https://doi.org/10.1016/j.palaeo.2005.06.019.
- Panchuk, K.M., Holmden, C.E., Leslie, S.A., 2006. Local controls on carbon cycling in the Ordovician Midcontinent region of North America, with implications for carbon isotope secular curves. J. Sediment. Res. 76, 200–211. https://doi.org/10. 2110/jsr.2006.017.
- Peters, S.E., Husson, J.M., 2017. Sediment cycling on continental and oceanic crust. Geology 45, 323–326. https://doi.org/10.1130/G38861.1.
- Petersen, S.V., Tabor, C.R., Lohmann, K.C., Poulsen, C.J., Meyer, K.W., Carpenter, S.J., Erickson, J.M., Matsunaga, K.K.S., Smith, S.Y., Sheldon, N.D., 2016. Temperature and salinity of the late cretaceous western interior seaway. Geology 44, 903–906. https://doi.org/10.1130/G38311.1.
- Pörtner, H.O., 2002. Climate variations and the physiological basis of temperature dependent biogeography: systemic to molecular hierarchy of thermal tolerance in animals. Comp. Biochem. Physiol. 132, 739–761. https://doi.org/10.1016/S1095-6433(02)00045-4.
- Pucéat, E., Joachimski, M.M., Bouilloux, A., Monna, F., Bonin, A., Motreuil, S., Morinière, P., Hénard, S., Mourin, J., Dera, G., Quesne, D., 2010. Revised phosphate-water fractionation equation reassessing paleotemperatures derived from biogenic apatite. Earth Planet. Sci. Lett. 298, 135–142. https://doi.org/10.1016/j.epsl.2010.07.034.
- Richey, J.D., Montañez, I.P., Goddéris, Y., Looy, C.V., Griffis, N.P., William, A., 2020. Influence of temporally varying weatherability on CO_2 -climate coupling and

- ecosystem change in the late Paleozoic. Clim. Past Discuss. 1 (37). https://doi.org/10.5194/cp-2020-50.
- Roark, A., Flake, R., Grossman, E.L., Olszewski, T., Lebold, J., Thomas, D., Marcantonio, F., Miller, B., Raymond, A., Yancey, T., 2017. Brachiopod geochemical records from across the Carboniferous seas of North America: evidence for salinity gradients, stratification, and circulation patterns. Palaeogeogr. Palaeoclimatol. Palaeoecol. 485, 136–153. https://doi.org/10.1016/j.palaeo.2017.06.009.
- Rosenau, N.A., Tabor, N.J., Herrmann, A.D., 2014. Assessing the paleoenvironmental significance of middle-late Pennsylvanian conodont apatite ¹⁸O values in the Illinois Basin. Palaios 29, 250–265. https://doi.org/10.2110/palo.2013.112.
- Ryb, U., Eiler, J.M., 2018. Oxygen isotope composition of the Phanerozoic ocean and a possible solution to the dolomite problem 115, 1–6. https://doi.org/10.1073/pnas.1719681115.
- Rygel, M.C., Fielding, C.R., Frank, T.D., Birgenheier, L.P., 2008. The magnitude of late Paleozoic glacioeustatic fluctuations: a synthesis. J. Sediment. Res. 78, 500–511. https://doi.org/10.2110/jsr.2008.058.
- Sun, Q., Whitney, M.M., Bryan, F.O., Tseng, Y. heng, 2019. Assessing the skill of the improved treatment of riverine freshwater in the Community Earth System Model (CESM) relative to a new salinity climatology. J. Adv. Model. Earth Syst. 2. https://doi.org/10.1029/2018MS001349.
- Tabor, C.R., Otto-bliesner, B.L., Brady, E.C., Nusbaumer, J., Erb, M.P., Wong, T.E., Liu, Z., Noone, D., 2018. Interpreting precession-driven δ^{18} O variability in the South Asian monsoon region. J. Geophys. Res., Atmos., 5927–5946. https://doi.org/10.1029/2018|D028424.
- Tseng, Y. heng, Bryan, F.O., Whitney, M.M., 2016. Impacts of the representation of riverine freshwater input in the community earth system model. Ocean Model. 105, 71–86. https://doi.org/10.1016/j.ocemod.2016.08.002.
- Turner, A.C.E., Algeo, T.J., Peng, Y., Herrmann, A.D., 2019. Circulation patterns in the Late Pennsylvanian North American Midcontinent Sea inferred from spatial gradients in sediment chemistry and mineralogy. Palaeogeogr. Palaeoclimatol. Palaeoecol. 531. https://doi.org/10.1016/j.palaeo.2018.12.008.
- van Geldern, R., Joachimski, M.M., Day, J., Jansen, U., Alvarez, F., Yolkin, E.A., Ma, X.P., 2006. Carbon, oxygen and strontium isotope records of Devonian brachiopod shell calcite. Palaeogeogr. Palaeoclimatol. Palaeoecol. https://doi.org/10.1016/j.palaeo.2006.03.045.
- Veizer, J., Prokoph, A., 2015. Temperatures and oxygen isotopic composition of Phanerozoic oceans. Earth-Sci. Rev. 146, 92–104. https://doi.org/10.1016/j. earscirev.2015.03.008.
- Waelbroeck, C., Paul, A., Kucera, M., Rosell-Melé, A., Weinelt, M., Schneider, R., Mix, A.C., Abelmann, A., Armand, L., Bard, E., Barker, S., Barrows, T.T., Benway, H., Cacho, I., Chen, M.T., Cortijo, E., Crosta, X., De Vernal, A., Dokken, T., Duprat, J., Elderfield, H., Eynaud, F., Gersonde, R., Hayes, A., Henry, M., Hillaire-Marcel, C., Huang, C.C., Jansen, E., Juggins, S., Kallel, N., Kiefer, T., Kienast, M., Labeyrie, L., Leclaire, H., Londeix, L., Mangin, S., Matthiessen, J., Marret, F., Meland, M., Morey, A.E., Mulitza, S., Pflaumann, U., Pisias, N.G., Radi, T., Rochon, A., Rohling, E.J., Sbaffi, L., Schäfer-Neth, C., Solignac, S., Spero, H., Tachikawa, K., Turon, J.L., 2009. Constraints on the magnitude and patterns of ocean cooling at the Last Glacial Maximum. Nat. Geosci. 2, 127–132. https://doi.org/10.1038/ngeo411.
- Wilson, J.P., Montañez, I.P., White, J.D., DiMichele, W.A., McElwain, J.C., Poulsen, C.J., Hren, M.T., 2017. Dynamic Carboniferous tropical forests: new views of plant function and potential for physiological forcing of climate. New Phytol. 215, 1333–1353. https://doi.org/10.1111/nph.14700.
- Woodard, S.C., Thomas, D.J., Grossman, E.L., Olszewski, T.D., Yancey, T.E., Miller, B.V., Raymond, A., 2013. Radiogenic isotope composition of Carboniferous seawater from North American epicontinental seas. Palaeogeogr. Palaeoclimatol. Palaeoecol. 370, 51–63. https://doi.org/10.1016/j.palaeo.2012.11.018.
- Zhu, J., Liu, Z., Brady, E., Otto-Bliesner, B., Zhang, J., Noone, D., Tomas, R., Nusbaumer, J., Wong, T., Jahn, A., Tabor, C., 2017. Reduced ENSO variability at the LGM revealed by an isotope-enabled Earth system model. Geophys. Res. Lett. 44, 6984–6992. https://doi.org/10.1002/2017GL073406.
- Zhu, J., Poulsen, C.J., Otto-Bliesner, B.L., Liu, Z., Brady, E.C., Noone, D.C., 2020. Simulation of early Eocene water isotopes using an Earth system model and its implication for past climate reconstruction. Earth Planet. Sci. Lett. 537, 116164. https://doi.org/10.1016/j.epsl.2020.116164.
- Ziegler, A., 1985. Paleogeographic interpretation: with an example from the mid-Cretaceous. Annu. Rev. Earth Planet. Sci. 13, 385–425. https://doi.org/10.1146/ annurey.earth.13.1.385.